














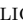


X-RAY POLARIZATION OF THE MAGNETAR 1E 1841–045 IN OUTBURST

RACHAEL STEWART ¹, GEORGE YOUNES ^{2,3}, ALICE K. HARDING ⁴, ZORAWAR WADIASINGH ^{5,2,6},
MATTHEW G. BARING ⁷, MICHELA NEGRO ⁸, TOD E. STROHMAYER ², WYNN C. G. HO ⁹, MASON NG ^{10,11},
ZAVEN ARZOUMANIAN,² HOA DINH THI ⁷, NICCOLÒ DI LALLA ¹², TERUAKI ENOTO ¹³, KEITH GENDREAU ²,
CHIN-PING HU ¹⁴, ALEX VAN KOOTEN ¹, CHRYSsa KOUVELIOTOU ¹ AND ALEXANDER MCEWEN³

¹*Department of Physics, The George Washington University, Washington, DC 20052, USA*

²*Astrophysics Science Division, NASA Goddard Space Flight Center, Greenbelt, MD 20771, USA*

³*Center for Space Sciences and Technology, University of Maryland, Baltimore County, Baltimore, MD 21250, USA*

⁴*Theoretical Division, Los Alamos National Laboratory, Los Alamos, NM 87545, USA*

⁵*Department of Astronomy, University of Maryland, College Park, Maryland 20742, USA*

⁶*Center for Research and Exploration in Space Science and Technology, NASA/GSFC, Greenbelt, Maryland 20771, USA*

⁷*Department of Physics and Astronomy - MS 108, Rice University, 6100 Main Street, Houston, Texas 77251-1892, USA*

⁸*Department of Physics & Astronomy, Louisiana State University, Baton Rouge, LA 70803, USA*

⁹*Department of Physics and Astronomy, Haverford College, 370 Lancaster Avenue, Haverford, PA 19041, USA*

¹⁰*Department of Physics, McGill University, 3600 rue University, Montréal, QC H3A 2T8, Canada*

¹¹*Trottier Space Institute, McGill University, 3550 rue University, Montréal, QC H3A 2A7, Canada*

¹²*W. W. Hansen Experimental Physics Laboratory, Kauli Institute for Particle Astrophysics and Cosmology, Department of Physics and SLAC National Accelerator Laboratory, Stanford University, Stanford, CA 94305, USA*

¹³*RIKEN Cluster for Pioneering Research, 2-1 Hirosawa, Wako, Saitama 351-0198, Japan*

¹⁴*Department of Physics, National Changhua University of Education, Changhua 50007, Taiwan*

ABSTRACT

We report on *IXPE* and *NuSTAR* observations that began forty days following the onset of the 2024 outburst of the magnetar 1E 1841–045, marking the first ever *IXPE* observation of a magnetar in an enhanced state. Our spectropolarimetric analysis indicates that a non-thermal double power-law (PL) spectral model can fit the phase-averaged intensity data well, with the soft and hard components dominating below and above around 5 keV, respectively. We find that the soft PL exhibits a polarization degree (PD) of about 20% while the hard X-ray PL displays a PD of about 50%; both components have a polarization angle (PA) compatible with 0°. These results are supported through model-independent polarization analysis which shows an increasing PD from about 15% to 70% in the 2 – 3 keV and 6 – 8 keV ranges, respectively, while the PA remains consistent with 0°. We find marginal evidence for variability in the polarization properties with pulse phase, namely a higher PD at spin phases coinciding with the peak in the hard X-ray pulse. We compare the hard X-ray PL to the expectation from direct resonant inverse Compton scattering (RICS) and secondary pair cascade synchrotron radiation from primary high-energy RICS photons, finding that both can provide reasonable spectropolarimetric agreement with the data, yet, the latter more naturally. Finally, we suggest that the soft power law X-ray component may be emission emanating from a Comptonized corona in the inner magnetosphere.

Keywords: Magnetars — Neutron stars — X-rays — Pulsars — Polarimetry

1. INTRODUCTION

Magnetars are endowed with the strongest magnetic fields among the neutron star population, often surpassing 10^{14} G (Kouveliotou et al. 1998). This magnetic energy reservoir is evident through the magnetar’s bright persistent X-ray emission, unique bursting abilities, and outburst epochs spanning months to years (see, e.g.,

Turolla et al. 2015; Kaspi & Beloborodov 2017, for a review). Additionally, due to the presence of such large B-fields, the X-ray radiation emanating from magnetars is expected to be highly polarized (Gnedin & Sunyaev 1974; Meszaros et al. 1988; Heyl & Shaviv 2000, 2002; van Adelsberg & Perna 2009; Taverna et al. 2020), either in the ordinary (O) mode or the extraordinary mode

(X), parallel or perpendicular to the plane of the magnetic field and photon wave vector, respectively. Exotic quantum electrodynamics (QED) effects in magnetar regimes are also expected to play a significant role in shaping their polarization characteristics, such as vacuum birefringence (Meszaros 1992; Harding & Lai 2006) and mode conversion (Lai & Ho 2003; van Adelsberg & Lai 2006; Yatabe & Yamada 2017; Lai 2023), among others. Lastly, such polarization properties are highly energy- and phase-dependent, and a function of surface properties (gaseous versus condensate) and composition (see, e.g., Taverna & Turolla 2024, for a review).

Magnetars in quiescence and in outburst typically exhibit multiple spectral components: a thermal blackbody-like component (generally below 2 keV), a soft power law and a hard power law (generally above 5 keV). The blackbody (BB) component has been modeled as a magnetized atmosphere (see, e.g., van Adelsberg & Lai 2006) or as condensed surface emission (van Adelsberg et al. 2005; Potekhin et al. 2012). The soft power law (SPL) component may be due to Comptonization of atmosphere radiation by a corona just above the neutron star surface or resonant scattering by mildly relativistic electrons at higher altitude (Nobili et al. 2008a). The hard power law (HPL) component has been attributed to resonant inverse Compton scattering by relativistic electrons (Baring & Harding 2007) or to annihilation bremsstrahlung by a dense, trans-relativistic pair plasma (Thompson & Kostenko 2020). While spectral and timing information alone are limited in their ability to discriminate between these models, their distinctive polarization characteristics, when confronted with observations, could provide critical information for their true contribution, which in turn help distinguish competing models.

The persistently bright magnetar 1E 1841–045, located at approximately 8.5 kpc (Tian & Leahy 2008, revised to 5.8 ± 0.3 kpc by Ranasinghe & Leahy 2018) in the center of the X-ray and radio supernova remnant (SNR) Kes 73, has an inferred surface dipolar magnetic field of about 6.9×10^{14} G at the equator, one of the largest among the population (Vasisht & Gotthelf 1997). The source also exhibits a bright hard X-ray tail, which extends to > 200 keV (Kuiper et al. 2004, see also Enoto et al. 2017; An et al. 2013, 2015). Since its discovery, the source has displayed sporadic bursting activity on several occasions (Kumar & Safi-Harb 2010; Lin et al. 2011b; Dib & Kaspi 2014). Yet, no enhanced emission to its quiescent flux has ever been confirmed following these bursting episodes (Lin et al. 2011b; Dib & Kaspi 2014). On 2024 August 21, *Swift*’s Burst Alert Telescope (*BAT*) reported the detection of bursting activity

from 1E 1841–045 starting at 19:01:18 UT (Dichiara & Palmer 2024), later corroborated with *Fermi*’s Gamma-ray Burst Monitor (*GBM*) and the Neutron star Interior Composition Explorer (*NICER*) (Roberts et al. 2024; Ng et al. 2024), among other high energy instruments. *NICER*, *Swift*’s X-Ray Telescope (*XRT*), and Nuclear Spectroscopic Telescope ARray (*NuSTAR*) observations 8 days following the initial report revealed that the source 2–70 keV flux increased by a factor 2 and that the soft and hard X-ray pulse shape noticeably changed to a multi-peaked structure (Younes et al. 2024). These observations confirmed that the source is undergoing a radiative outburst in conjunction to its bursting activity, its first confirmed outburst.

In this paper, we report the polarimetric and spectropolarimetric results from the magnetar 1E 1841–045 during its 2024 outburst epoch, through the analysis of a simultaneous Imaging X-ray Polarimetry Explorer (*IXPE*) and *NuSTAR* observation, taken between September 28 and October 10, 40–50 days following its outburst onset (Dichiara & Palmer 2024). At the time of the observation, the source flux was still 40% elevated compared to its baseline emission, predominantly in the hard X-ray tail, and its pulse profile displayed evident variation compared to quiescence. This is the first time that *IXPE* has observed a magnetar in an enhanced flux state, contrasting with all its previous magnetar observations (e.g., Taverna et al. 2022; Lai 2023; Zane et al. 2023; Turolla et al. 2023; Heyl et al. 2024). Section 2 summarizes the observations and data reduction procedures. Section 3 details our findings. Section 4 discusses our results in the context of radiation processes in high B-field regime. We note that a companion paper also details the analysis of the *IXPE* and *NuSTAR* data while presenting a slightly different approach to the spectropolarimetry part (Rigoselli et al. 2024). The results and theoretical interpretation are largely consistent, except for the discussion on the nature of the soft X-ray component, where the two papers present distinct interpretive elements.

2. OBSERVATIONS AND DATA REDUCTION

The Imaging X-ray Polarimetry Explorer (*IXPE*) consists of three identical telescopes, each equipped with a Detector Unit (DU) that houses a Gas Pixel Detector and is sensitive in the 2–8 keV energy range (Weisskopf et al. 2022; Baldini et al. 2021). *IXPE* observed the magnetar 1E 1841–045 for 170 ks from 2024 September 28 to October 1 and for 130 ks from October 7 to October 10. The total livetime for the observation is about 292.5 ks.

We perform the data cleaning, region selection, and analysis utilizing the software `ixpeobssim` v.31.0.1 (Baldini et al. 2022). We set the instrument response functions (IRFs) to `ixpe:obssim20240701:v13` from `ixpeobssim`'s pseudo-CALDB which contains the `arf`, `rmf`, PSF, vignetting functions, modulation factors, and modulation responses corresponding to the observation date (Baldini et al. 2022). We applied the solar-system barycenter correction utilizing the HEASoft tool `barycorr` and best-known source coordinates (280.3275732°, -4.9339910°; Wachter et al. 2004).

We derive the rotational phase of each photon using CRIMP¹ (Code for Rotational-analysis of Isolated Magnetars and Pulsars) and a timing solution covering the entirety of 2024 (Younes et al. in prep). The `ixpeobssim` task `xpselect` was used to specify the energy and phase bins used in creating the energy- and phase-resolved data products, e.g., the event files and pulse profiles. Lastly, we use `xpbin` to extract all binned products, including the pulse profiles, polarization cubes, and PHA1, PHA1Q, and PHA1U spectra. For spectropolarimetry, we utilize Xspec version 12.14.0c, part of HEASOFT 6.33.1, to perform the spectral fitting.

We generate and examine radial profiles in order to select extraction region sizes that suitably maximize the signal-to-noise ratio of the source while minimizing the contribution from the surrounding SNR. We select a 30'' circular region for the source and an annulus of 60'' and 120'' for the background inner and outer radii, respectively, centered on the brightest pixel. The latter encompasses emission predominantly from the SNR, in addition to the cosmic background. Its area-normalized flux contributes 12%, 5%, and <2% to the point source flux at the 2–3 keV, 3–4 keV, 4–8 keV ranges, respectively. The modest elevated contribution at lower energies is due to the SNR emission. Moreover, the normalized Stokes parameters Q/I and U/I show no significant polarization signal from the SNR² with the measured PD falling under the $MDP_{99} \sim 13\%$. Hence, we deem that the contamination from the SNR to the magnetar emission is negligible, and that subtraction of the SNR + cosmic contribution from the polarization cubes and spectra is a sufficient treatment of the background for the remainder of this analysis.

We performed a search for short bursts in the *IXPE* data. We identify one candidate at 60581.431488977745

MJD (TDB), with a total number of 8 counts in a 22 ms bin. This is highly unlikely to occur by chance according to a Poisson probability density given the source rate of ~ 0.1 cts/s. We eliminate this time interval in our analysis. The background rejection outlined by Di Marco et al. (2023) disproportionately cut photons compatible with the location of the magnetar, especially at the higher energies between 6 and 8 keV, rejecting up to 10% of the source photons. On the other hand, at low energies, the background rejection does not improve the polarization detection significantly. We therefore opted to not apply the background rejection for this source (see the Appendix for more details). We similarly abstained from performing solar deflaring since the rejection did not improve the S/N but sacrificed a non-trivial number of counts.

The Nuclear Spectroscopic Telescope ARray (*NuSTAR*; Harrison et al. 2013) observed 1E 1841–045 on 2024 September 28 with a 50 ks exposure (observation ID 91001335002), simultaneous with the first leg of the *IXPE* observation. *NuSTAR* consists of two identical focal plane modules, FPMA and FPMB. We utilize *NuSTARDAS* software version 2.1.2 to clean and calibrate the event files. We employed the task `nuproducts` to extract source events, light curves, and spectra from a circular region with a 30''-radius around the source central brightest pixel. For the background region, we extract an annulus centered around the source with inner and outer radii of 60'' and 120'', respectively, which encompasses part of the SNR contribution and cosmic background.

The Neutron star Interior Composition Explorer (*NICER*) is a non-imaging, soft X-ray telescope mounted on the International Space Station, with a $\approx 6'$ diameter field-of-view (FoV; Gendreau et al. 2016), and with a collecting area peaking at 1900 cm² at 1.5 keV and a timing resolution < 300 ns. We cleaned and calibrated all *NICER* data utilizing *NICERDAS* version v12 as part of *HEASoft* version 6.33. We applied the standard filtering criteria utilizing the task `nicer12`. We compared light curves (binned with a 5 second resolution) created in the energy range 2–8 keV (where the source is expected to dominate the emission) to ones created in the 12–15 keV energy range. Almost all the counts in the latter band are due to high energy particle background. We eliminated any simultaneous flaring background intervals that appeared in both light curves. For this paper, we only present the pre-outburst *NICER* data covering the February to August 2024 period for comparison purposes with the post-outburst simultaneous *IXPE* and *NuSTAR* data.

¹<https://github.com/georgeyounes/CRIMP/tree/main>

²We are referring to the linear polarization in reference to the celestial north direction. We tested the presence of radial and tangential polarization in the SNR region finding values below the $MDP_{99} \sim 8\%$.

3. RESULTS

3.1. Polarization Characteristics

Figure 1 shows the phase-averaged Q and U stokes parameters from the combined DUs measured in different energy bands with the circle marking the 68.3% confidence level. The phase- and energy-integrated polarization angle (PA) is $1 \pm 3^\circ$ east of north, and the polarization degree (PD) from 2 – 8 keV is $31 \pm 4\%$. This measured polarization degree is large, comparable to that of 1RXS J170849.0–400910, which has the strongest measured phase- and energy-averaged polarization signal among the magnetar population to date (Zane et al. 2023, Taverna & Turolla 2024).

We find higher polarization degrees by binning the data according to four energy bands, i.e. 2–3, 3–4, 4–6, and 6–8 keV. This energy-resolved analysis reveals that the polarization degree increases monotonically according to energy, from $20 \pm 4\%$ at 2–3 keV up to $\approx 75 \pm 20\%$ at 6–8 keV (Figure 1). Meanwhile, the PA remains consistent with 0° across all energy bands. We note that all energy-dependent polarization values surpass the 99% C.L. minimum detectable polarization (MDP_{99}) at the corresponding energies.

Figure 2 shows the *IXPE*+*NuSTAR* post-outburst pulse profiles (second, third, and fourth panels). The pulse profile of 1E 1841–045 preceding the outburst as observed with *NICER* is also displayed (upper panel). Each pulse profile uses 32 bins and is normalized by its average. Two cycles are shown for clarity. The pulse profile morphology of 1E 1841–045 clearly evolves following the outburst. The soft X-ray (e.g. 2–8, 3–10 keV) main pulse peak narrows in width while a sub-peak emerges on its leading edge. The hard X-ray 10–70 keV post-outburst pulse profile, while broad, peaks at a phase coincident with the shoulder observed at lower energies. This pulse shape is slightly different when compared to historical *NuSTAR* profiles which mainly show a flat-top pulse (An et al. 2013, 2015, and Younes et al. in prep.).

The upper panels of Figure 3 shows the *IXPE* pulse profiles in three energy bands 2 – 4, 4 – 8, and 2 – 8 keV. We present the corresponding phase-resolved polarization degree and angle in a select five phase bins in the middle and lower panels, respectively. These phase-bins were chosen to correspond to the morphological features of the pulse, namely, the newly-formed subpeak (red-shaded region), main pulse (blue-shaded region), shoulder (purple- and orange-shaded regions) and the pulse minimum (green-shaded region). We note that the purple and orange-shaded regions coincide with the pulse-maximum of the hard 10–70 keV X-ray band.

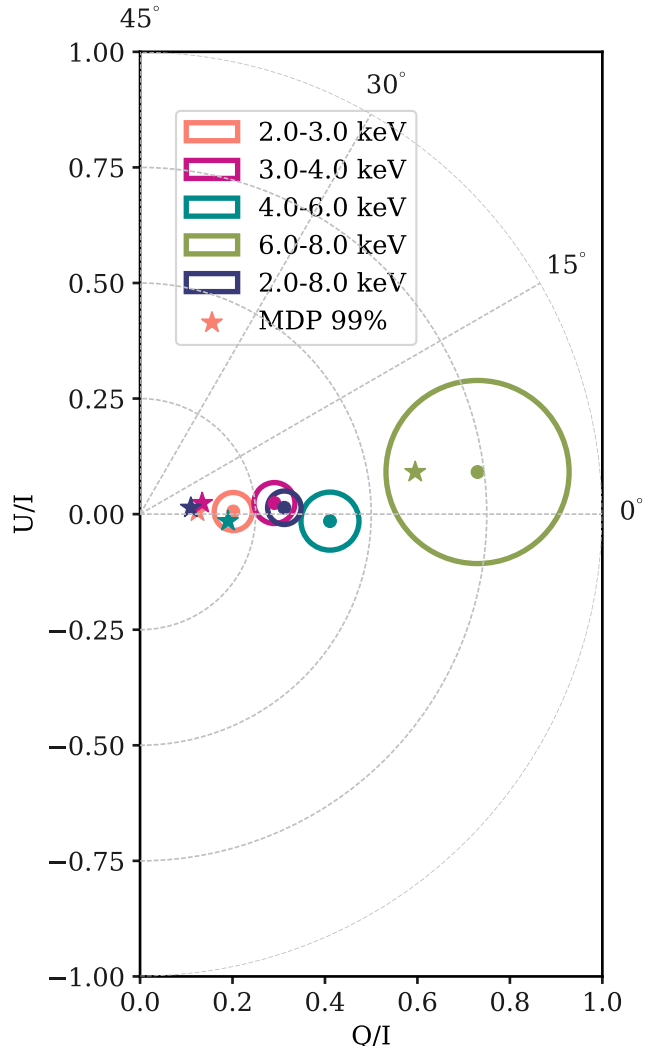


Figure 1. The background-subtracted, phase-averaged polarization characteristics of 1E 1841–045 according to 4 energy bins. Contours show the 68.3% (1σ) confidence regions for both polarization degree and angle. Stars show the corresponding MDP_{99} for each energy band. The energy-integrated polarization is shown in dark blue.

The horizontal shaded areas in the polarization degree panels display the MDP_{99} for each phase bin at each corresponding energy.

The phase-resolved polarization degree of the 2–8 keV band surpasses the MDP_{99} at each bin with the exception of the pulse minimum (in green). The polarization degree exhibits small variability between 20–40%, with the PD minimum aligned with the intensity pulse profile minimum and the maximum with the trailing shoulder (shown in purple and orange), which corresponds to the hard X-ray peak. Only mild variation is detected in the polarization angle, with the value remaining largely consistent with 0° at each phase bin.

3.2. Spectropolarimetry

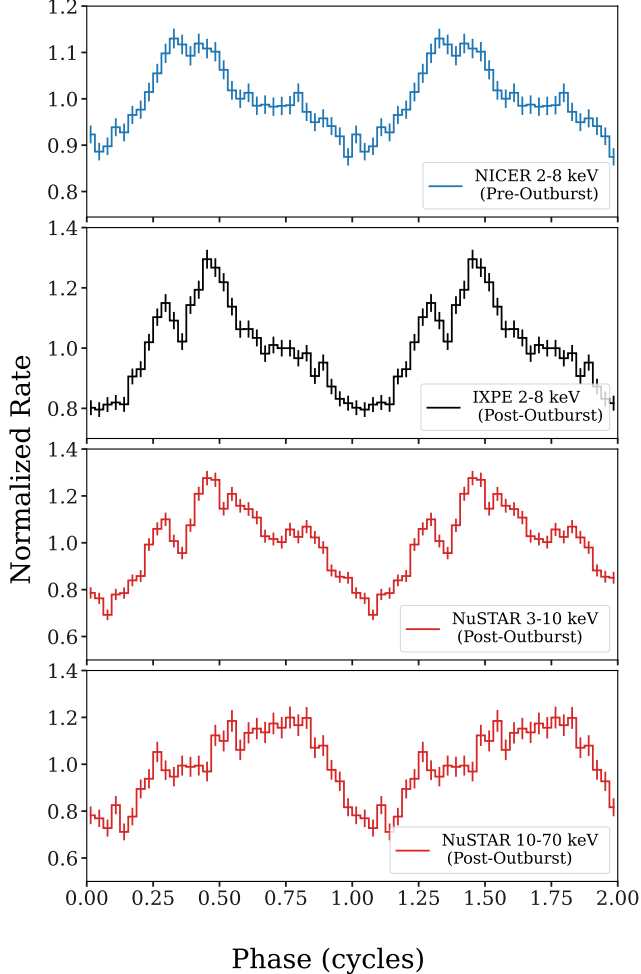


Figure 2. *Upper Panel:* The normalized intensity pulse profile of 1E 1841–045 from 2 – 8 keV using observations from *NICER* preceding the outburst. *Second Panel:* The source 2-8 keV intensity pulse profile post-outburst as observed with *IXPE*. *Third Panel:* The *NuSTAR* pulse profile from 3 – 10 keV simultaneous to *IXPE*. *Bottom Panel:* The *NuSTAR* 10-70 keV pulse profile.

In the 2–4 keV range, only the phase bin corresponding to the orange band exceeds the MDP_{99} . Therefore, the statistics are not robust enough to assert a definitive phase-dependence for the 2–4 keV band. The polarization angle at each phase bin also maintains around 0° .

The 4–8 keV polarization degree shows mild variation between $\sim 30\%$ and 60% but is primarily consistent within uncertainties. The 4–8 keV PD peak coincides with the peak of the *NuSTAR* 10–70 keV pulse profile (see Figure 2). The polarization angle varies from around 0° up to 30° at the intensity pulse minimum, albeit with large uncertainties.

To gain insights into the spectral behavior of the polarization characteristics, we used *Xspec* (Arnaud 1996) to simultaneously fit the *NuSTAR* spectra in the 3–70 keV and the *IXPE* spectra in the 2–8 keV range. For the *NuSTAR* observations, we grouped each spectra to have 5 counts per bin and used the W-statistic (`cstat` in *Xspec*); likewise for the *IXPE* data, we grouped the spectra according to 25 counts per bin and used chi-squared statistics. Due to the *NuSTAR* and *IXPE*’s limited sensitivity to the neutral hydrogen column density in the direction of the source, we fix N_{H} to the historical value of $2.6 \times 10^{22} \text{ cm}^{-2}$ as derived with *Chandra* (Kumar & Safi-Harb 2010). We likewise use the Anders & Grevesse elemental abundances (`angr` in *Xspec*, Anders & Grevesse 1989) for consistency along with the photo-electric cross-sections of Verner et al. (1996) and the Tuebingen-Boulder ISM absorption model (`tbabs`). Lastly, we add a multiplicative constant component to the spectral models to take into account any calibration uncertainty between the *NuSTAR* FPM detectors and the *IXPE* DUs. This constant also encompasses the difference in the SNR contribution to the *IXPE* data, in which it can be largely resolved, compared to *NuSTAR* where it is blended with the source point spread function. We find the calibration constants for *IXPE* to be about 70% that of *NuSTAR* for each spectral model tested (see Table 1).

We fit the *NuSTAR*+*IXPE* intensity spectral data to a double power-law (2PL) model. We find that this model results in a statistically acceptable fit with a total fit statistic of 2037 with 2138 degrees of freedom (dof). The best-fit νF_ν models of each component are shown in the upper left panel of Figure 4. The corresponding data-to-model ratio is shown in the middle left panel. We tried to add a third component to our double PL model, namely a blackbody (BB) component. Yet, when leaving all component parameters free to vary, we cannot constrain the extra BB model parameters, and the fit results do not significantly improve compared to the 2PL model. We also attempted to fit the data with an absorbed BB and PL model. This model fit resulted in an adequate total fit statistic of 2197 with 2138 dof but is disfavored compared to the 2PL model fit. Moreover, the corresponding data-to-model ratio residuals display strong systematic deviation from unity as shown in the lower left panel of Figure 4. Lastly, we added a second BB component to the latter model. This 2BB and PL model describes the data well with a total fit statistic of 2019 for 2136 dof. In the following, we provide a discussion on the spectropolarimetry results from these two models, starting with the 2PL one.

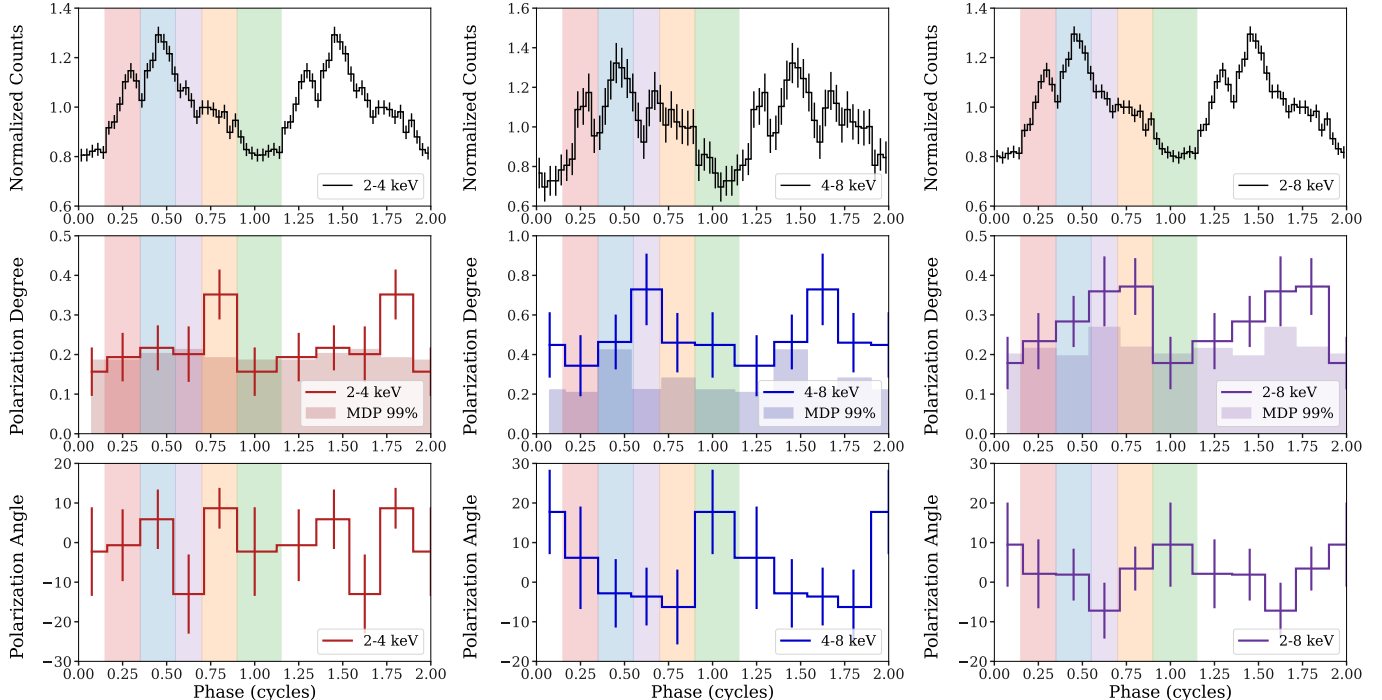


Figure 3. Phase-resolved polarization characteristics of 1E 1841–045. The columns display the intensity pulse profiles (top row), polarization degree (center), and polarization angle (bottom row) according to 2–4 keV (left column), 4–8 keV (central column), and 2–8 keV (right column). The phaseograms are divided according to five phase bins (shown in colored vertical bands) that correspond to morphological features of the *IXPE* energy-integrated intensity pulse profile. The corresponding MDP₉₉ for each phase and energy bin are shown as overlapping shaded regions.

To probe the polarization properties of the 2PL best-fit spectral components, we fit the Q and U spectra alongside the *NuSTAR*+*IXPE* intensity spectra utilizing a constant polarization model (`polconst` in `Xspec`). We let all intensity and polarization parameters freely vary, with the exception of N_{H} . We show the phase-averaged Q and U Stokes spectra on the right-hand side of Figure 4. We obtain a soft PL photon index of $\Gamma_{\text{SPL}} = 3.84 \pm 0.04$ and a hard PL photon index of $\Gamma_{\text{HPL}} = 1.23 \pm 0.02$ (see Table 1 for the best-fit spectral parameters). The total unabsorbed 2–70 keV flux is $1.05 \pm 0.01 \times 10^{-10} \text{ erg s}^{-1} \text{ cm}^{-2}$, approximately 40% larger when compared to the historic value (An et al. 2013, Younes et al. in prep.). The soft PL dominates the emission up to 5 keV, above which the emission from the hard X-ray tail becomes more prominent (Figure 4). We find a polarization degree of $17 \pm 6\%$ for the soft PL and $51 \pm 10\%$ for the hard PL. Additionally the polarization angle lies within 1σ of 0° for both components.

For the 2BB+PL model, we find a cool and a hot BB temperature of $0.414 \pm 0.003 \text{ keV}$ and $1.03 \pm 0.06 \text{ keV}$, respectively, along with emitting areas of about $139 \pm 15 \text{ km}^2$ and $0.58 \pm 0.14 \text{ km}^2$ assuming a distance of 8.5 kpc. We find a photon index $\Gamma = 1.34 \pm 0.02$. We cannot constrain the polarization properties of all three compo-

nents simultaneously. Hence, we assumed that the PD of one of the components is 0, namely the hot BB. If we assume the cool BB or the PL, which dominates at the lower and higher energy parts of the spectrum, respectively, to have $\text{PD} = 0\%$, we find that the hot BB will exhibit a 100% polarization in order to compensate for the lack of polarization signature at either end of the spectrum, which we consider nonphysical. Under the assumption of an unpolarized hot BB, we find that the cool BB and the PL have a PD of $15 \pm 6\%$ and $57 \pm 9\%$, respectively. The PA of both components are consistent with 0° at the 1σ level.

4. DISCUSSION

We have presented the detailed spectropolarimetric analysis of the first magnetar observed by *IXPE* (and *NuSTAR*) in an outburst, 1E 1841–045. These observations occurred while the source still exhibited a 40% increase in flux mainly driven by the presence of an enhanced hard X-ray tail, which dominates the emission at energies $\gtrsim 5 \text{ keV}$, well within the *IXPE* band. We explored various models to describe the spectral decomposition of the *IXPE*+*NuSTAR* data. Both a 2PL and 2BB+PL models performed similarly well in capturing the broadband spectral shape. The spectro-polarimetric results for both fits are comparable, with the key distinc-

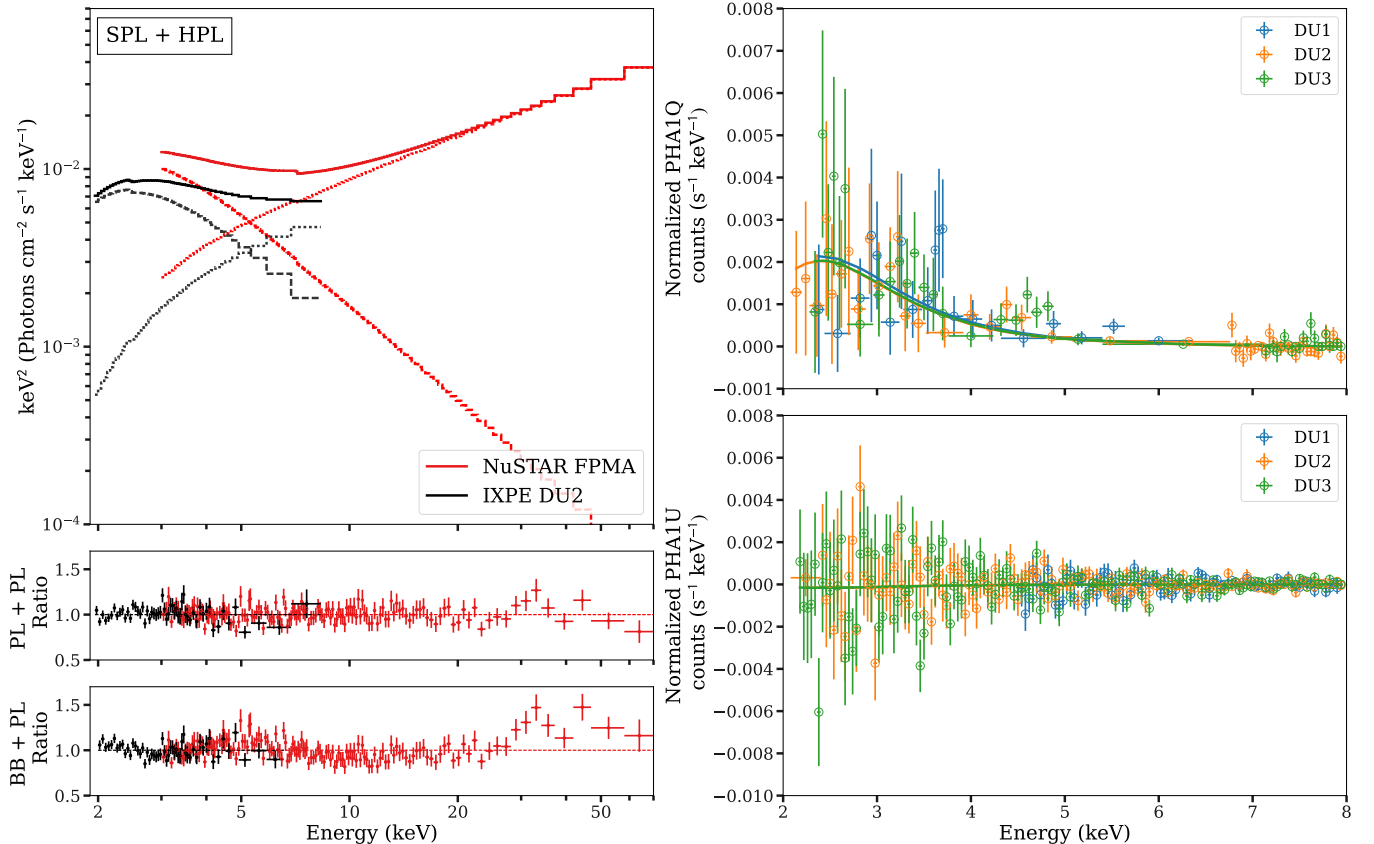


Figure 4. The joint spectral νF_ν models of the simultaneous *NuSTAR*+*IXPE* observation. The upper left panel shows the best fit model of `constant*tbabs(polconst*powerlaw+polconst*powerlaw)`. Note: Only *NuSTAR* FPMA and *DU2* are displayed to enhance visual clarity. The central left panel shows the data divided by the folded model for the absorbed 2PL model; the bottom left panel shows the ratio between the data and the folded model for an absorbed BB+PL for comparison. The right panels show the normalized Stokes Q (top) and U (bottom) spectra for the 3 *IXPE* DUs with the solid lines showing the best fit model in linear space. Best-fit spectral parameters can be found in Table 1.

tion being the nature of the soft-energy spectral component as either thermal or non-thermal, albeit, both resulting in a comparable PD of about 20%. Additionally, both spectral models indicate that the hard X-ray tail is highly polarized with $PD \approx 50\%$. The PA of both components align at $\approx 0^\circ$. Given that the emission of the hard X-ray tail is likely a combination of the quiescent and enhanced emission, it is noteworthy that the measured polarization achieves such high values. It may indicate that the locale of the outburst emission originates from a similar site as the persistent emission (likely close to the equatorial region from twisted dipolar field lines), showcasing how polarization measurements can constrain the emission topology of magnetars in outbursts. We note that the above results are fully supported in our model-independent, energy-resolved findings in which the PD increases with energy from about 15% to 70% in the 2 – 8 keV range, while the PA remains constant at 0° . Lastly, phase-resolved analysis shows marginal (2σ) variation in PD with spin-phase in

the 2–8 keV range with the maximum PD aligning with the trailing shoulder of the main pulse (i.e., where the peak of the hard X-ray pulse falls), and the minimum PD is observed at pulse minimum. Our polarimetry results for 1E 1841–045 display similar trends to those derived for the magnetar 1RXS J170849.0–400910, yet with two significant differences; in the latter (1) a soft X-ray component dominates throughout the *IXPE* band (Zane et al. 2023, Stewart et al. in prep.), and (2) the PD displays a clear anti-correlation with the intensity pulse profile. These differences might be due to differing emission components (or emission contributions) in the 2 – 8 keV range as observed in these two sources. Additionally, the fact that 1E 1841–045 was observed in an enhanced state while 1RXS J1708 remained quiescent may contribute to these differences as well.

4.1. Nature of the soft X-ray emission

The 2PL fits presented suggest a steep PL for the spectrum below around 5 keV, which is consistent with pre-

Model Parameter	Value $\pm 1\sigma$
N_{H} (cm^{-2})	2.6×10^{22} (fixed)
PD _{SPL}	0.17 ± 0.06
PA _{SPL} (deg)	-3 ± 10
SPL Photon Index	3.84 ± 0.04
SPL Γ norm	0.113 ± 0.005
PD _{HPL}	0.5 ± 0.1
PA _{HPL} (deg)	-1 ± 7
HPL Photon Index	1.23 ± 0.02
HPL Γ norm	0.0016 ± 0.0001
C _{FPMA}	1.0 (fixed)
C _{FPMB}	1.04 ± 0.01
C _{DU1}	0.73 ± 0.01
C _{DU2}	0.68 ± 0.01
C _{DU3}	0.70 ± 0.01
2PL Total Fit Statistic	2037 with 2138 d.o.f.

Table 1. Spectral parameters for the best fit model, an absorbed soft power-law (SPL) + hard power-law (HPL) obtained using Xspec’s model `tbabs*(powerlaw * polconst + powerlaw * polconst)`. A multiplicative cross-calibration uncertainty was also added to the model. All uncertainties are calculated at the 68.3% confidence level. The fit statistic employs a combination of the C-stat and Chi-Squared statistics used for *NuSTAR* and *IXPE*, respectively.

vious spectral analyses of the source (An et al. 2013, 2015). This soft component could be described by a Comptonization scenario such as that which leads to the Kompaneets equation broadly applied to coronae proximate to accretion disks. In this picture, which was invoked in the context of bursts from the magnetar SGR J0501+4516 by Lin et al. (2011a), soft, thermal X rays from the surface would be upscattered repeatedly by non-relativistic or mildly-relativistic electrons heated within a corona in the inner magnetosphere relatively close to the star (less than ten stellar radii, R_{NS}). In such proximity, the cyclotron resonance to the Compton cross section (e.g., Canuto et al. 1971; Herold 1979; Daugherty & Harding 1986) would reside in the gamma-ray band and so the scatterings would be non-resonant, contrasting the repeated resonant cyclotron scattering model of Lyutikov & Gavriil (2006); Nobili et al. (2008b); Caiazzo et al. (2022) for heating photons that can apply at higher altitudes, typically at radii of $20R_{\text{NS}}$ or more. The origin of the heating of the electrons is presumably similar to (but less intense than) that for the short duration bursts, perhaps Alfvén wave driven or some other form of energy injection and dissipation in the inner magnetosphere.

To assess if this Comptonization scenario is possibly viable, let n_e be the number density of such electrons,

$\langle\gamma_e\rangle \sim 1$ be their mean Lorentz factor, and $\epsilon_{\text{rad}} < 1$ be the efficiency of them radiating (i.e., transferring their energy to the photons) in the magnetosphere close to the surface. The observed steep power-law X-ray luminosity then satisfies $L_X \sim \epsilon_{\text{rad}} \langle\gamma_e\rangle m_e c^2 (4\pi n_e R^2 c)$ for a Comptonization zone of size R , an estimate detailed in Baring & Harding (2007), which yields number densities $n_e \sim 3 \times 10^{17} L_{X,35} / [\epsilon_{\text{rad}} \langle\gamma_e\rangle] \text{ cm}^{-3}$ for scaled luminosities $L_{X,35} \equiv L_X / 10^{35} \text{ erg/sec}$, if $R \sim 10^6 \text{ cm}$. Therefore large densities are needed, and one quickly discerns that non-magnetic Thomson optical depths of $\tau_T = n_e \sigma_T R \gtrsim 1$ are possible and even likely if $\epsilon_{\text{rad}} \sim 0.01 - 0.1$, thereby demonstrating the baseline viability of the Comptonization picture.

Comparing the magnetospheric charge density en_e with the classic Goldreich & Julian (1969) value of $\rho_{\text{GJ}} = \nabla \cdot \mathbf{E} / 4\pi = -\boldsymbol{\Omega} \cdot \mathbf{B} / (2\pi c)$ for force-free, magnetohydrodynamic rotators, one arrives at the following ratio for a magnetic dipole configuration

$$\frac{en_e}{|\rho_{\text{GJ}}|} \approx \frac{4,670}{\epsilon_{\text{rad}} \langle\gamma_e\rangle} \frac{L_{X,35} P}{B_{15} R_6^2} . \quad (1)$$

This result is expressed using magnetar pulse periods P in units of seconds, surface polar magnetic fields B_{15} in units of 10^{15} Gauss, and emission region sizes R_6 in units of 10^6 cm . Accordingly, the requisite density n_e is highly super-Goldreich-Julian. One can also compare with expectations for densities needed for twisted magnetosphere models (Thompson et al. 2002; Beloborodov & Thompson 2007). Since these demand sufficient charge current densities \mathbf{j}_{tw} to enhance the magnetic field above the dipolar values \mathbf{B}_{dip} , the requisite densities $n_e = |\mathbf{j}_{\text{tw}}| / (ec)$ are most simply estimated using Ampère’s law, $\nabla \times \mathbf{B}_{\text{tw}} = -(4\pi/c)\mathbf{j}_{\text{tw}}$. Thus, near the stellar surface, the twisted field has a magnitude $|\mathbf{B}_{\text{tw}}| \sim (4\pi R/c)|\mathbf{j}_{\text{tw}}| = 4\pi en_e R$. Clearly, Eq. (1) constitutes the ratio $|\mathbf{j}_{\text{tw}}| / |\rho_{\text{GJ}}|$ of the twist to Goldreich-Julian currents. Accordingly, one can approximately couple the ratio of the strengths of the twisted and dipolar fields to the X-ray luminosity:

$$\frac{|\mathbf{B}_{\text{tw}}|}{|\mathbf{B}_{\text{dip}}|} \sim \frac{4\pi R}{Pc} \frac{en_e}{|\rho_{\text{GJ}}|} \sim \frac{2}{\epsilon_{\text{rad}} \langle\gamma_e\rangle} \frac{L_{X,35}}{B_{15} R_6} . \quad (2)$$

For the observed value of $L_{X,35} \sim 2.5$ in the 2 – 4 keV band, and the polar field $B_{15} \approx 1.4$ for 1E 1841–045, we deduce that a strong twist with $|\mathbf{B}_{\text{tw}}| \gtrsim |\mathbf{B}_{\text{dip}}|$ is commensurate with the observed luminosity for the steep power-law component during this elevated state.

The textbook solutions to the Kompaneets equation for non-magnetic Comptonization (e.g., Rybicki & Lightman 1979) yield a power-law spectral index that couples to the Compton y -parameter $y =$

$4kT_e/(m_e c^2) \max\{\tau_T, \tau_T^2\}$. Specifically, for an electron temperature $T_e \ll m_e c^2/k$, the differential spectrum for non-thermal photon energies E in the range $kT_\gamma \lesssim E \ll kT_e$ is

$$\frac{dN_\gamma}{dE} \propto E^{-\Gamma} \quad , \quad \Gamma = -\frac{1}{2} + \sqrt{\frac{9}{4} + \frac{4}{y}} \quad . \quad (3)$$

This form applies for parameters $y < 1$. The index captures the competition between energy gain imparted to photons ($4kT_e$ per scattering) and the escape of photons from the Comptonization region. The steep power-law index determined for the two power law fits has an index of $\Gamma \approx 3.84$, which corresponds to $y \approx 0.24$. This is an acceptable value, corresponding to unsaturated Comptonization. If the coronal electrons have a temperature as low as $kT_e \sim 10$ keV, then the Thomson optical depth would be $\tau_T \sim 1.75$; lower values of τ_T would be realized for higher T_e . It must be noted that the strong magnetic field will impact the Comptonization process, modifying the y -parameter and altering the index, since it introduces anisotropy and polarization-dependence into the scattering process, thereby changing both the energy increase and the escape probability per scattering. The combination of these influences leads to a modest steepening of the spectrum, i.e., a degradation of the Comptonization efficiency by the magnetic field (Cecco-bello et al. 2014).

The strong magnetic field critically influences the polarization and anisotropy signatures. For non-resonant Comptonization, scatterings involving ordinary propagation states (O-modes, \parallel polarization) dominate the emission region's opacity; the extraordinary modes (X-modes, \perp polarization) scatter extremely infrequently (e.g., Canuto et al. 1971; Herold 1979). This establishes a strong suppression of emission perpendicular to the local field, leading to most radiation emerging from the scattering zone close to the local field direction (e.g., see Figure 2 of Hu et al. 2022). For such directions, the disparity between scattering cross sections of the O and X modes is much more limited (e.g., Barchas et al. 2021), leading to modest polarization degrees (PDs) below or well below 50% (Hu et al. 2022, ; Figure 2). These strongly contrast the $\sim 100\%$ PDs evident at other viewing directions to the field. Accordingly, one expects that the steep Comptonization spectrum would exhibit significant but moderate polarization, the value of which would need to be determined by a detailed geometrical construction embedded in a full magnetic scattering transfer simulation. As both modes have cross sections well below the Thomson value in these focal directions, the radiative efficiency ϵ_{rad} drops accordingly, and to maintain moderate overall opacity and total luminosity,

the electron density in the region must increase correspondingly.

For a spatially-extended Comptonization region, observers would preferentially select signals from locales where \mathbf{B} points close to the line of sight as the magnetar rotates. Thus, it is anticipated that neither the PD nor angle would vary substantially with pulse phase; this is what is exhibited in Fig. 3 for the 2–4 keV band. Furthermore, strong field line twists establish a field geometry resembling a split monopole morphology with \mathbf{B} again roughly aligning with the radial direction to an observer. While this indicates general polarimetric consistency of the Comptonization picture with the 1E 1841–045 data, we do expect that the repeated resonant cyclotron scattering model at higher altitudes will display similarly modest polarization levels, due to the relative equity of the resonant cross sections for the two eigenmodes.

As an alternative to the steep PL picture, the thermal model (2BB) that describes the soft part of the *IXPE* spectrum is similar to the two component blackbody spectral models that are fit to the magnetars with previous *IXPE* polarization measurements, 4U 0142+61 (Taverna et al. 2022) and 1RXS J170849.0–400910 (Zane et al. 2023). These works argued that the surface of these two magnetars is in a condensed state, and the measured polarization degree and angle are due in part to emission from this condensed surface. On the other hand, an alternative explanation is that the polarization measurements are due to the effect of QED birefringence and mode conversion in a strong magnetized heavy element atmosphere (Lai 2023). Unfortunately, the observations presented here for 1E 1841–045 cannot discriminate between these two explanations. One reason is that the magnetic field of 1E 1841–045 is stronger than that of the other two magnetars, especially that of 4U 0142+61, such that mode conversion in 1E 1841–045 can produce high PD and no change in polarization angle, while condensation of part of the surface is also plausible with the inferred temperature of the large cool component (Medin & Lai 2007, also see accompanying paper for more details on this scenario). Moreover, the observations of 1E 1841–045 are taken during an outburst, with possible contamination from differing components, while those of 4U 0142+61 and 1RXS J170849.0–400910 occurred in quiescence.

4.2. Interpretation of the Hard X-ray Tail

4.2.1. Resonant Inverse Compton Scattering

The non-thermal emission that starts dominating at energies $\gtrsim 5$ keV and extends to 70 keV demands a non-thermal particle population. This hard X-ray compo-

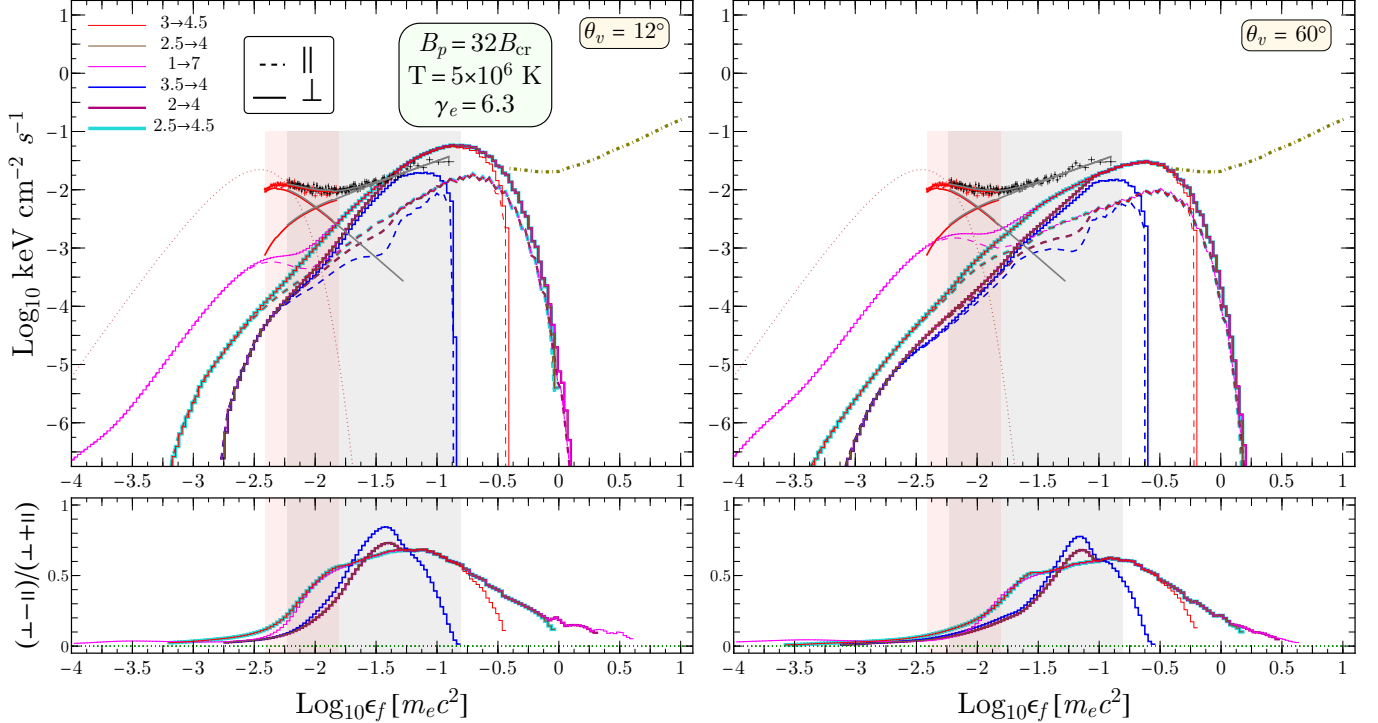


Figure 5. Pure RICS model spectra, without splitting attenuation or cascades, integrated over toroidal volumes as indicated ranges of field footpoint altitudes in units of stellar radii, e.g. $r_{\max} \in \{2^3, 2^{4.5}\}$ in red. A blackbody with appropriate area and $T = 5 \times 10^6$ K is plotted in dotted red. The left and right panels depict viewing angles of $\theta_v = \{12^\circ, 60^\circ\}$ with respect to the magnetic pole, as indicated. The bottom row depicts the polarization degree, which traces the \perp mode preferentially resulting from scattering, which map to solid and dashed curves in the upper panel. *IXPE* and *NuSTAR* data for 1E 1841–045 are plotted and the energy ranges of the two instruments are indicated with relevant shading. The brown dash-dot curve depicts the 2 yr continuum sensitivity for *COSI* (Tomsick et al. 2023).

ment is pulsed with a broad profile and thus likely arises from low altitudes in the magnetosphere, i.e. much nearer to the rotating star than to its light cylinder.

The most efficient radiative process for generating such hard X-ray tails in magnetars is resonant inverse Compton scattering (RICS, Baring & Harding 2007; Fernández & Thompson 2007). Large photon densities originating from the surface bathe the inner magnetosphere, and relativistic electrons/positrons can scatter these soft X-rays to higher energies (Baring & Harding 2007; Baring et al. 2011). The cross section is resonant at the cyclotron energy in the electron rest frame (ERF) (Herold 1979; Bussard et al. 1986; Daugherty & Harding 1986), with the scattering of photons in the \perp (X-mode) state generally exceeding that of the \parallel (O-mode) in head-on scatterings in the ERF. Lorentz transformations and scattering kinematics lead to a strong angle dependence of the RICS rates, and yield a profound anisotropy in emission due to Doppler beaming. The resonance is always accessible in the thermal photon bath, and leads to a characteristic hard, flat power-law spectrum for even monoenergetic electrons (Wadi-

asingh et al. 2018). Moreover, the resonance access condition leads to a direct mapping between observed photon energies at particular viewing directions and associated locales in the magnetosphere. For a rotating magnetar, the emission anisotropy generates pulsation, and the pulse fraction increases with photon energy, as is observed for the non-thermal hard X-rays of several magnetars. Yet, we note that the generation of broad pulse profiles generally requires lower Lorentz factors $\gamma_e \sim 10 - 30$.

Wadiasingh et al. (2018) predominantly considered RICS with relativistic charges confined to single field loops and monoenergetic electrons and found model spectra were too hard to match the data of persistent hard X-ray emission of the sample of quiescent magnetars. Toroidal shells of field loops steepen the spectra, yet usually not enough to accommodate magnetar observations. This motivated more recent studies (first presented in Wadiasingh et al. 2019) which consider ensembles of relativistic charges in the magnetosphere over extended volumes. This appears sufficient to soften pure RICS spectra for even higher particle energies $\gamma_e \sim 100$.

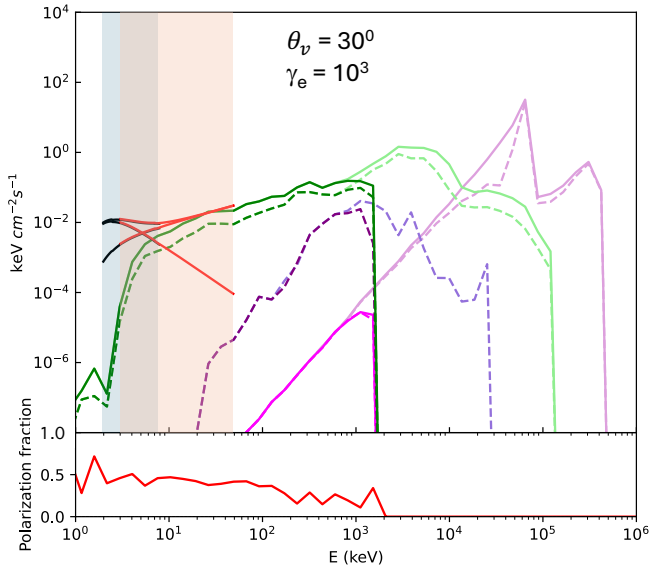


Figure 6. Top panel: Model photon spectra for O-mode (dashed lines) and X-mode (solid lines) modes from RICS (pink), splitting (purple) and pair synchrotron (green) from a pair cascade from electrons on a closed magnetic field loop with $r_{\max} = 6$ neutron star radii, surface magnetic field strength $B = 32 B_{\text{cr}}$, viewing angle, $\theta_v = 30^\circ$, scattering photons from the whole neutron star surface with temperature 5×10^6 K. Light lines are unattenuated spectra and dark lines are attenuated (observed) spectra. The normalization is arbitrary. The solid black/red lines are the soft, hard and total model fits of *IXPE*/*NuSTAR* data. The *IXPE* model has been multiplied by a factor of 1.4 to correct for the calibration uncertainty with *NuSTAR*. Bottom panel: polarization degree of the total attenuated spectrum.

The accompanying generation of much more energetic photons then may lead to significant attenuation and cascading by single photon pair production and photon splitting (Baring & Harding 2001). Moreover, high altitude large angle scattering may result in a low-energy component below 10 keV that is largely unpolarized. The domain of pure RICS emission as a possible explanation for magnetar hard tails is therefore primarily for lower Lorentz factors where gamma-ray attenuation and pair cascading are not relevant.

In Figure 5 we present computations of pure RICS model spectra (Wadiasingh et al., in prep.) for a relatively low Lorentz factor of $\gamma_e \approx 6.3$ depicting various volume ranges, expressed in log base-2 maximum height of a loop in units of stellar radius, $\log_2 r_{\max}$, i.e. $1 \rightarrow 7$ expresses a large toroidal volume from the equator to footpoints attaining 128 stellar radii. Here θ_v is the instantaneous angle of the observer with respect to the magnetic pole, and the choice of parameters reflects the character of 1E 1841–045 with $B_p \approx 32 B_{\text{cr}}$, where $B_{\text{cr}} \approx 4.41 \times 10^{13}$ G is the quan-

tum critical field, and $T \sim 5 \times 10^6$ K. One can see for some ranges of such toroidal volumes, particularly the range of $\log_2 r_{\max} \sim 3 - 4.5$ a high polarization degree of 30 – 70% in the *IXPE* band may be attained by pure RICS. Notable in the models is the polarization degree that is increasing with energy, similar to that observed. This selection is marginally compatible with the *NuSTAR* power law, although it predicts a spectral cutoff right at the edge of the *NuSTAR* band. Choosing more extended volumes, larger viewing angles to the magnetic axis, or higher Lorentz factors in zones of activation can result in higher energy emission, potentially extending to the *COSI* band (Tomsick et al. 2023) although accompanied by a generally lower polarization degree in the *IXPE* band.

4.2.2. Synchrotron radiation from pair cascades

The RICS radiation on closed field lines from relativistic electrons (of higher Lorentz factors than considered in Figure 5) with Lorentz factors $\gamma_e > 10 - 100$ will be attenuated by one-photon pair production and photon splitting (Baring & Harding 2001). In near-surface magnetar fields, $B_0 > 0.2 B_{\text{cr}}$, the pairs are produced very near the threshold, $2m_e c^2 / \sin \theta_{\text{kB}}$, where θ_{kB} is the angle between the photon momentum and local field. However, if the closed loops extend to altitudes of several stellar radii, the local magnetic field will drop to values that allow the pairs to be produced in higher excited states. Photon splitting (Adler et al. 1970) does not have a threshold, so that the RICS spectra can be attenuated below pair threshold. If the weak-dispersion regime applies in magnetar fields, then the only allowed splitting mode is the X-mode \rightarrow O-mode O-mode. In this limit, photons polarized in X-mode split before reaching pair threshold and O-mode photons pair produce. The electron-positron pairs that are produced in excited Landau levels will radiate synchrotron photons of lower energy. Those photons together with the split photons will add components to the total radiation spectrum.

Figure 6 shows the resulting spectrum at a particular viewing angle, $\theta_v = 30^\circ$, from a Monte-Carlo simulation of a pair cascade (Harding et al. in prep) initiated by electrons with Lorentz factor $\gamma_e = 10^3$ on a closed field loop with maximum radius $r_{\max} = 6 R_{\text{NS}}$. The surface magnetic field strength is $B_p = 32 B_{\text{cr}}$, to match that of 1E 1841–045 and the neutron star whole-surface temperature is 5×10^6 K. RICS, splitting and synchrotron radiation components are all visible. Since the radiation at this observer angle comes from electrons approaching the top of the field loop, the local magnetic field $B \sim 0.08 B_{\text{cr}}$ where splitting is no longer dominant and both photon polarization modes for all

spectral components are attenuated by pair production. The RICS spectrum and the split photon spectrum are quite hard but with the pairs produced in high Landau states, the synchrotron spectrum overwhelms both and is much softer. The synchrotron spectrum extends from the high-energy cutoff near 2 MeV down to around 3–4 keV, with X-mode photons dominating. The polarization degree is near 50% up to about 100–200 keV at which point the photon splitting spectrum, dominated by O-mode photons, begins to contribute. Also plotted are the *IXPE* and *NuSTAR* model soft and hard power law fits as well as the total model spectrum. The hard power law model matches the pair synchrotron spectrum well for this viewing angle. The synchrotron component is present at all viewing angles for these parameters but its spectral index varies, being softer at larger viewing angles. Although the model shown in Figure 6 assumes that the electrons do not suffer any RICS energy losses, in cases where they do lose energy there are still dominant synchrotron components with similar photon index and polarization (Harding et al. in prep).

ACKNOWLEDGMENTS

The authors are grateful to the *IXPE* team for approving their DDT observation request of 1E 1841–045. The authors also thank the *NuSTAR* team for approving the DDT observation simultaneous to *IXPE* and the *NICER* team for continuing with the yearly magnetar monitoring program. A portion of this work was supported by NASA through the *NICER* mission and the Astrophysics Explorers Program. R.S. is partly funded through NASA grants 80NSSC21K1997, 80NSSC23K1114, and 80NSSC22K0853 (PI G.Y.). The material is based upon work supported by NASA under award number 80GSFC21M0002. M.G.B. thanks NASA for generous support under awards 80NSSC22K0777 and 80NSSC22K1576. W.C.G.H. acknowledges support through grant 80NSSC23K0078 from NASA. M. Ng is a Fonds de Recherche du Quebec – Nature et Technologies (FRQNT) postdoctoral fellow.

REFERENCES

- Adler, S. L., Bahcall, J. N., Callan, C. G., & Rosenbluth, M. N. 1970, *Physical Review Letters*, 25, 1061 [4.2.2](#)
- An, H., Archibald, R. F., Hascoët, R., et al. 2015, *ApJ*, 807, 93 [1](#), [3.1](#), [4.1](#)
- An, H., Hascoët, R., Kaspi, V. M., et al. 2013, *ApJ*, 779, 163 [1](#), [3.1](#), [3.2](#), [4.1](#)
- Anders, E. & Grevesse, N. 1989, *GeoCoA*, 53, 197 [3.2](#)
- Arnaud, K. A. 1996, in *ASP Conf. Ser. 101: Astronomical Data Analysis Software and Systems V*, 17 [3.2](#)
- Baldini, L., Barbanera, M., Bellazzini, R., et al. 2021, *Astroparticle Physics*, 133, 102628 [2](#)
- Baldini, L., Bucciantini, N., Lalla, N. D., et al. 2022, *SoftwareX*, 19, 101194 [2](#)
- Barchas, J. A., Hu, K., & Baring, M. G. 2021, *MNRAS*, 500, 5369 [4.1](#)
- Baring, M. G. & Harding, A. K. 2001, *ApJ*, 547, 929 [4.2.1](#), [4.2.2](#)
- Baring, M. G. & Harding, A. K. 2007, *Ap&SS*, 308, 109 [1](#), [4.1](#), [4.2.1](#)
- Baring, M. G., Wadiasingh, Z., & Gonthier, P. L. 2011, *ApJ*, 733, 61 [4.2.1](#)
- Beloborodov, A. M. & Thompson, C. 2007, *ApJ*, 657, 967 [4.1](#)
- Bussard, R. W., Alexander, S. B., & Meszaros, P. 1986, *PhRvD*, 34, 440 [4.2.1](#)
- Caiazzo, I., González-Caniulef, D., Heyl, J., & Fernández, R. 2022, *MNRAS*, 514, 5024 [4.1](#)
- Canuto, V., Lodenguai, J., & Ruderman, M. 1971, *PhRvD*, 3, 2303 [4.1](#), [4.1](#)
- Ceccobello, C., Farinelli, R., & Titarchuk, L. 2014, *A&A*, 562, A99 [4.1](#)
- Daugherty, J. K. & Harding, A. K. 1986, *ApJ*, 309, 362 [4.1](#), [4.2.1](#)
- Di Marco, A., Soffitta, P., Costa, E., et al. 2023, *AJ*, 165, 143 [2](#), [7](#), [A](#)
- Dib, R. & Kaspi, V. M. 2014, *ApJ*, 784, 37 [1](#)
- Dichiara, S. & Palmer, D. M. 2024, *The Astronomer’s Telegram*, 16784, 1 [1](#)
- Enoto, T., Shibata, S., Kitaguchi, T., et al. 2017, *ApJS*, 231, 8 [1](#)
- Fernández, R. & Thompson, C. 2007, *ApJ*, 660, 615 [4.2.1](#)
- Gendreau, K. C., Arzoumanian, Z., Adkins, P. W., et al. 2016, *Society of Photo-Optical Instrumentation Engineers (SPIE) Conference Series*, Vol. 9905, *The Neutron star Interior Composition Explorer (NICER): design and development*, 99051H [2](#)
- Gnedin, I. N. & Sunyaev, R. A. 1974, *A&A*, 36, 379 [1](#)
- Goldreich, P. & Julian, W. H. 1969, *ApJ*, 157, 869 [4.1](#)
- Harding, A. K. & Lai, D. 2006, *Reports on Progress in Physics*, 69, 2631 [1](#)
- Harrison, F. A., Craig, W. W., Christensen, F. E., et al. 2013, *ApJ*, 770, 103 [2](#)
- Herold, H. 1979, *PhRvD*, 19, 2868 [4.1](#), [4.1](#), [4.2.1](#)

- Heyl, J., Taverna, R., Turolla, R., et al. 2024, *MNRAS*, 527, 12219 [1](#)
- Heyl, J. S. & Shaviv, N. J. 2000, *MNRAS*, 311, 555 [1](#)
- Heyl, J. S. & Shaviv, N. J. 2002, *PhRvD*, 66, 023002 [1](#)
- Hu, K., Baring, M. G., Barchas, J. A., & Younes, G. 2022, *ApJ*, 928, 82 [4.1](#)
- Kaspi, V. M. & Beloborodov, A. 2017, *ArXiv e-prints* [1](#)
- Kouveliotou, C., Dieters, S., Strohmayer, T., et al. 1998, *Nature*, 393, 235 [1](#)
- Kuiper, L., Hermsen, W., & Mendez, M. 2004, *ApJ*, 613, 1173 [1](#)
- Kumar, H. S. & Safi-Harb, S. 2010, *ApJL*, 725, L191 [1](#), [3.2](#)
- Lai, D. 2023, *Proceedings of the National Academy of Science*, 120, e2216534120 [1](#), [4.1](#)
- Lai, D. & Ho, W. C. 2003, *Physical Review Letters*, 91, 071101 [1](#)
- Lin, L., Kouveliotou, C., Baring, M. G., et al. 2011a, *ApJ*, 739, 87 [4.1](#)
- Lin, L., Kouveliotou, C., Göğüş, E., et al. 2011b, *ApJL*, 740, L16 [1](#)
- Lyutikov, M. & Gavriil, F. P. 2006, *MNRAS*, 368, 690 [4.1](#)
- Medin, Z. & Lai, D. 2007, *MNRAS*, 382, 1833 [4.1](#)
- Meszaros, P. 1992, *High-energy radiation from magnetized neutron stars* [1](#)
- Meszaros, P., Novick, R., Szentgyorgyi, A., Chanan, G. A., & Weisskopf, M. C. 1988, *ApJ*, 324, 1056 [1](#)
- Ng, M., Younes, G., Hu, C. P., et al. 2024, *The Astronomer's Telegram*, 16789, 1 [1](#)
- Nobili, L., Turolla, R., & Zane, S. 2008a, *MNRAS*, 386, 1527 [1](#)
- Nobili, L., Turolla, R., & Zane, S. 2008b, *MNRAS*, 386, 1527 [4.1](#)
- Potekhin, A. Y., Suleimanov, V. F., van Adelsberg, M., & Werner, K. 2012, *A&A*, 546, A121 [1](#)
- Ranasinghe, S. & Leahy, D. A. 2018, *AJ*, 155, 204 [1](#)
- Roberts, O. J., Veres, P., Barra, C. d., McDermott, P., & Dalessi, S. 2024, *The Astronomer's Telegram*, 16786, 1 [1](#)
- Rybicki, G. B. & Lightman, A. P. 1979, *Radiative processes in astrophysics* [4.1](#)
- Taverna, R. & Turolla, R. 2024, *Galaxies*, 12, 6 [1](#), [3.1](#)
- Taverna, R., Turolla, R., Muleri, F., et al. 2022, *Science*, 378, 646 [1](#), [4.1](#)
- Taverna, R., Turolla, R., Suleimanov, V., Potekhin, A. Y., & Zane, S. 2020, *MNRAS*, 492, 5057 [1](#)
- Thompson, C. & Kostenko, A. 2020, *ApJ*, 904, 184 [1](#)
- Thompson, C., Lyutikov, M., & Kulkarni, S. R. 2002, *ApJ*, 574, 332 [4.1](#)
- Tian, W. W. & Leahy, D. A. 2008, *ApJ*, 677, 292 [1](#)
- Tomsick, J. A., Boggs, S. E., Zoglauer, A., et al. 2023, *arXiv e-prints*, arXiv:2308.12362 [5](#), [4.2.1](#)
- Turolla, R., Taverna, R., Israel, G. L., et al. 2023, *ApJ*, 954, 88 [1](#)
- Turolla, R., Zane, S., & Watts, A. L. 2015, *Reports on Progress in Physics*, 78, 116901 [1](#)
- van Adelsberg, M. & Lai, D. 2006, *MNRAS*, 373, 1495 [1](#)
- van Adelsberg, M., Lai, D., Potekhin, A. Y., & Arras, P. 2005, *ApJ*, 628, 902 [1](#)
- van Adelsberg, M. & Perna, R. 2009, *MNRAS*, 399, 1523 [1](#)
- Vasisht, G. & Gotthelf, E. V. 1997, *ApJL*, 486, L129 [1](#)
- Verner, D. A., Ferland, G. J., Korista, K. T., & Yakovlev, D. G. 1996, *ApJ*, 465, 487 [3.2](#)
- Wachter, S., Patel, S. K., Kouveliotou, C., et al. 2004, *ApJ*, 615, 887 [2](#)
- Wadiasingh, Z., Baring, M. G., Gonthier, P. L., & Harding, A. K. 2018, *ApJ*, 854, 98 [4.2.1](#), [4.2.1](#)
- Wadiasingh, Z., Younes, G., Baring, M. G., et al. 2019, *BAAS*, 51, 292 [4.2.1](#)
- Weisskopf, M. C., Soffitta, P., Baldini, L., et al. 2022, *Journal of Astronomical Telescopes, Instruments, and Systems*, 8, 026002 [2](#)
- Yatabe, A. & Yamada, S. 2017, *ApJ*, 850, 185 [1](#)
- Younes, G., Hu, C. P., Enoto, T., et al. 2024, *The Astronomer's Telegram*, 16802, 1 [1](#)
- Zane, S., Taverna, R., González-Caniulef, D., et al. 2023, *ApJL*, 944, L27 [1](#), [3.1](#), [4](#), [4.1](#)

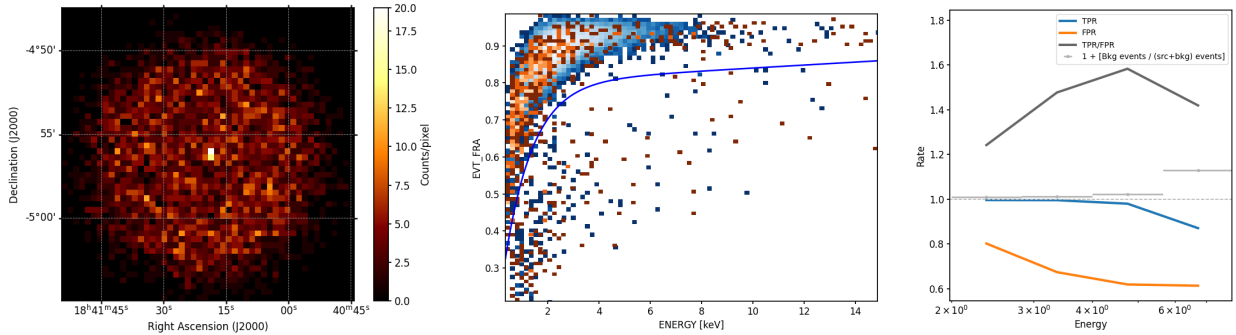


Figure 7. *Left:* Counts map of the rejected component by the cut devised in [Di Marco et al. \(2023\)](#). *Middle:* Heat maps (source region in blue shades, background region in red shades) of the energy fraction contained in the main cluster (EVT_FRA) of the event reconstructed in the detector as a function of the reconstructed energy; the blue line illustrates the background rejection cut, which removes all event below it. *Right:* False positive rate (FPR) and the true positive rate (TPR), defined as described in the text, in blue and orange respectively; the dark gray line corresponds to the ratio between the TPR and FPR; the light gray point shows the ratio between the number of counts in the background region and the source region in each energy bin (the ratio is scaled up by 1 for visualization purposes).

APPENDIX

A. BACKGROUND REJECTION CONSIDERATIONS

As mentioned in the manuscript we did not perform the instrumental background rejection procedure outlined in [Di Marco et al. \(2023\)](#). In this appendix we illustrate the reason behind this choice.

Fig. 7 (left panel) shows the rejected component in the FoV resulting from the background rejection in the 6-8 keV energy band. It is evident that the cut removes good photons from the source. The middle panel illustrates the background rejection cut in blue, which rejects all events below the curve defined in the space of the energy fraction contained in the main cluster (EVT_FRA) as a function of the reconstructed energy. The blue and red maps show the number of events in that parameter space within 30 arcsec regions around the target and a background-only region (far from the SNR). This plot shows how this cut becomes more and more inefficient with increasing energy, increasingly rejecting significant fraction of source events, while not removing most of the background events. This is also shown in the plot on the right panel of Fig. 7. Here we illustrate the *false positive rate* (FPR) and the *true positive rate* (TPR) defined as follows,

$$FPR = \frac{FP}{FP + TN} \quad TPR = \frac{TP}{TP + FN}, \quad (\text{A1})$$

where FP is the number of events in the background-only region we keep after the cut (false positives), TN is the number of events in the background-only region we reject with the cut (true negatives), TP is the number of events in the source region we keep after the cut (true positives), and FN is the number of events in the source region we reject with the cut (false negatives). Ideally one would like to maximize the TPR (the efficiency in keeping source events) while minimizing the FPR (the background contamination). It is evident that above 5 keV the cut becomes inefficient, lowering the true positive rate while not improving on the false positive rate. As mentioned in the text, below 5 keV the count statistics of the source is high, dominating over the instrumental background. We hence conclude that the background rejection cut is only beneficial but ineffective below 5 keV, while becoming increasingly counterproductive at higher energies, ultimately failing to improve the signal-to-background ratio. This led to the decision to not apply the background rejection procedure for the analysis of this *IXPE* observation, relying on the subtraction of the unpolarized SNR as background as a sufficient method to remove both instrumental and astrophysical background contamination (see Section 2).